$Ni_{12}P_5$ Nanoparticles as an Efficient Catalyst for Hydrogen Generation *via* Electrolysis and Photoelectrolysis

Zhipeng Huang,[†,*] Zhibo Chen,[†] Zhongzhong Chen,[†] Cuncai Lv,[†] Hua Meng,[‡] and Chi Zhang[†,*]

[†]Functional Molecular Materials Research Centre, Scientific Research Academy, Jiangsu University, Zhenjiang 212013, People's Republic of China, and [‡]Research Institute of Refrigeration and Thermal Engineering, College of Mechanical Engineering, Tongji University, Shanghai 200092, People's Republic of China

ABSTRACT The exploitation of a low-cost catalyst is desirable for hydrogen generation from electrolysis or photoelectrolysis. In this study we have demonstrated that nickel phosphide ($Ni_{12}P_5$) nanoparticles have efficient and stable catalytic activity for the hydrogen evolution reaction. The catalytic performance of $Ni_{12}P_5$ nanoparticles is favorably comparable to those of recently reported efficient nonprecious catalysts. The optimal overpotential required for 20 mA/cm^2 current density is 143 $\pm$ 3 mV in acidic solution (H_2SO_4, 0.5 M). The catalytic activity of $Ni_{12}P_5$ is likely to be correlated with the charged natures of Ni and P. $Ni_{12}P_5$ nanoparticles were introduced to silicon nanowires, and the power conversion efficiency of the resulting composite is larger than that of silicon nanowires decorated with platinum particles. This result demonstrates the promising application potential of metal phosphide in photoelectrochemical hydrogen generation.

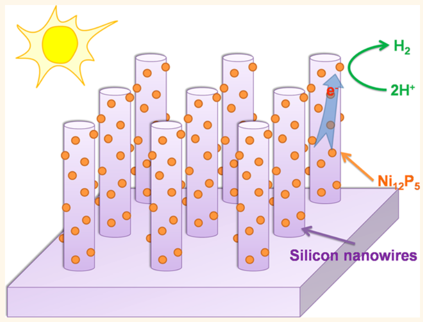

KEYWORDS: hydrogen generation · electrolysis · photoelectrolysis · nickel phosphide · silicon nanowires · electrocatalyst

The increasingly serious energy crisis and environmental issues have stimulated considerable research concerning renewable clean energy.[1,2] Solar-driven water splitting into hydrogen (H_2) is one of the most promising approaches to produce clean energy,[3−5] because it can harvest solar energy and store the energy as clean fuel (H_2), and the storage of energy in H_2 has the largest mass storage density and the longest storage time.[5] Efficient photoelectrochemical hydrogen generation requires the modification of a photocathode with an active catalyst for the hydrogen evolution reaction (HER), because of native slow HER kinetics at semiconductor surfaces. Although platinum and other noble metals have been successfully incorporated into photocathodes for hydrogen generation,[6−9] the widespread practical application of these HER catalysts is limited because of high cost and low abundance. Therefore, the exploitation of efficient photocathodes modified with a low-cost and effective HER catalyst is attracting extensive attention.

Recently reported nonprecious HER catalysts include molybdenum sulfide,[10,11] first-row transition metal dichalcogenides,[12,13] molybdenum carbide,[14,15] tungsten carbide,[16] nickel phosphide (Ni_2P),[17] cobalt phosphide (CoP),[18−20] and so on. The edge sites of molybdenum sulfide are analogous to the active centers of nitrogenase,[10] while some surface cations of the first-row transition metal dichalcogenides resemble the ligand number and symmetry of active centers in hydrogenase ([NiFe]-hydrogenase, [FeFe]-hydrogenase, or [Fe]-hydrogenase).[13] The electronic structures of group VI transition metal carbides are similar to those of Pt-group metals.[21] Metal (Ni or Co) and P in metal phosphide have similar charged natures to those of the hydride acceptor and proton acceptor in [NiFe] hydrogenase and its analogues.[22] These reports suggest that mimicking the coordination structures or electron structures of active sites of high-performance noble metal catalysts or hydrogenases is an efficient approach to the development of new nonprecious HER catalysts.

On the other hand, only limited kinds of nonprecious HER catalysts have been incorporated into photocathodes to promote solar-driven hydrogen generation (*e.g.*,

* Address correspondence to zhpuang@ujs.edu.cn; chizhang@ujs.edu.cn.

Received for review April 22, 2014 and accepted July 25, 2014.

Published online July 28, 2014
10.1021/nn5022204

molybdenum sulfide[23−26] and Ni−Mo particles[27,28]), although various nonprecious HER catalysts have been developed. In addition, photocathodes loaded with nonprecious HER catalysts have not yet demonstrated better hydrogen generation capability than the photocathodes loaded with Pt nanoparticles.

In this study, we report the promising application potential of nickel phosphide ($Ni_{12}P_5$) nanoparticles in hydrogen generation *via* electrolysis and photoelectrolysis. $Ni_{12}P_5$ nanoparticles show efficient HER catalytic activity, which is favorably comparable to those of recently reported nonprecious catalysts. The optimal overpotential required for 20 mA/cm^2 current density is 143 ± 3 mV in acidic solution. Implied by the similarity between the charged nature of Ni (and P) in $Ni_{12}P_5$ nanoparticles and that of the hydride acceptor (and proton acceptor) in [NiFe] hydrogenase and its analogues, the HER catalytic activity of $Ni_{12}P_5$ nanoparticles might be associated with electron structures of Ni and P. $Ni_{12}P_5$ nanoparticles were loaded on the surface of silicon nanowires (SiNWs) by convenient drop coating. The solar power conversion efficiency (PCE) of SiNWs modified with $Ni_{12}P_5$ nanoparticles (denoted as $Ni_{12}P_5$/SiNWs) is 2.98 ± 0.07%, which is larger than that of silicon nanowires modified with Pt particles (Pt/SiNWs). Our results demonstrate that metal phosphide can be used in solar-driven hydrogen generation and that the superior PCE of a photocathode can be achieved by silicon nanowires loaded with a nonprecious HER catalyst instead of with Pt.

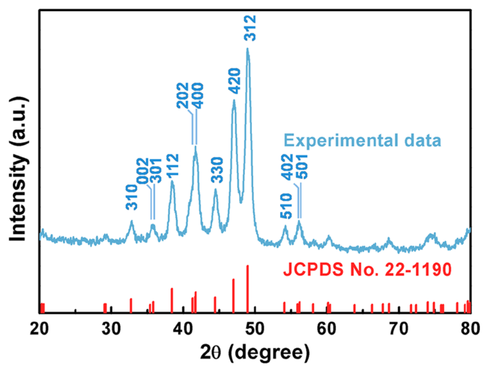

Figure 1. XRD pattern of $Ni_{12}P_5$.

RESULTS AND DISCUSSION

Nickel phosphide ($Ni_{12}P_5$) nanoparticles were synthesized by the reaction of nickel acetate tetrahydrate ($Ni(Ac)_2 \cdot 4H_2O$), triphenyl phosphine (TPP), and oleylamine (OLA) in a round beaker on a heating mantle (300 °C) for 30 min under nitrogen (N_2). The details of the synthesis method can be found in the Methods. TPP was adopted as a low-cost phosphorus source, and OLA acted as both a solvent and capping agent. The product was identified *via* an X-ray diffraction (XRD) experiment. The good crystallinity of product is revealed by distinct peaks in the XRD pattern (Figure 1). All peaks can be allocated to those of tetragonal phase $Ni_{12}P_5$ (JCPDS No. 22-1190), and no impurity phase can be found. The average diameter estimated from XRD pattern *via* the Scherrer equation[29] is 14.0 ± 0.6 nm (Table S1, Supporting Information). In addition, compositional information was determined by energy dispersive X-ray (EDX) spectroscopy (Figure S1, Supporting Information). The atomic ratio of Ni to P is measured to be 2.53:1, which is in accordance with that of stoichiometric $Ni_{12}P_5$ (2.4:1).

Transmission electron microscopy (TEM) characterization was carried out to scrutinize the morphology and detailed structure of $Ni_{12}P_5$. It is revealed that the resulting $Ni_{12}P_5$ is nearly spherical particles with 14.3 ± 2.0 nm diameter (Figure 2a and its inset). The average diameter obtained from the TEM image corresponds with that from the XRD pattern. The selected area electron diffraction (SAED) pattern of $Ni_{12}P_5$ particles is shown in Figure S2 (Supporting Information). The pattern can be indexed to tetragonal phase $Ni_{12}P_5$ (Table S2, Supporting Information). The microstructure of $Ni_{12}P_5$ nanoparticles was assessed by high-resolution TEM (HRTEM) observation. The single-crystalline nature

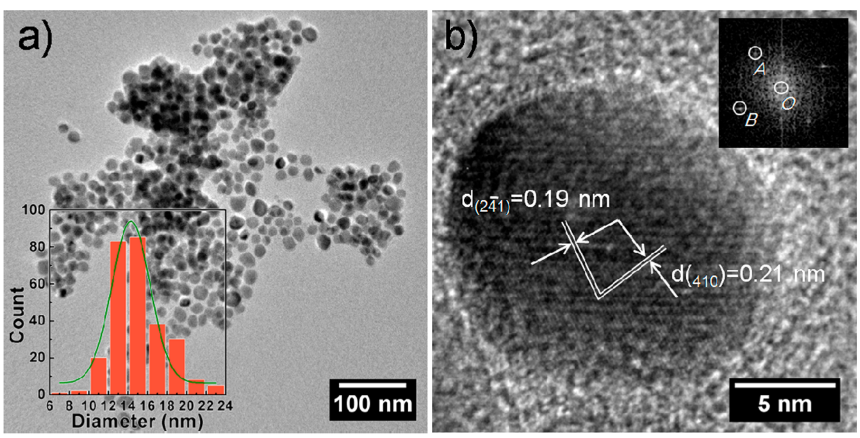

Figure 2. (a) TEM image of $Ni_{12}P_5$ nanoparticles. Inset of (a) shows the diameter distribution of $Ni_{12}P_5$ nanoparticles. (b) HRTEM image of a $Ni_{12}P_5$ nanoparticle. Inset of (b) shows FFT pattern of the $Ni_{12}P_5$ nanoparticle.

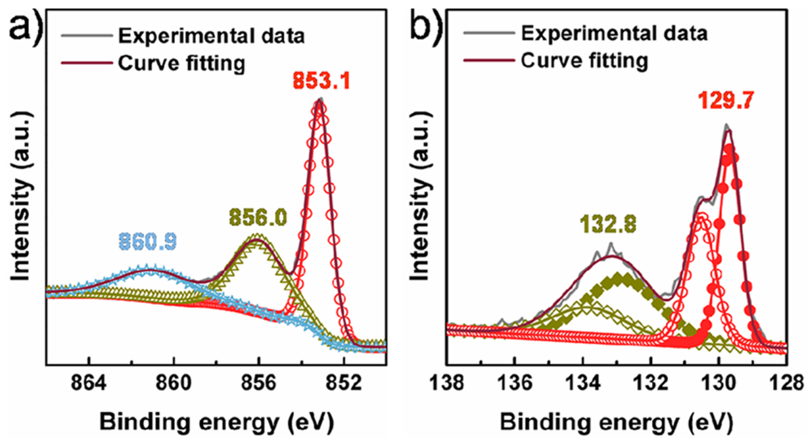

Figure 3. XPS spectra of (a) Ni $2p_{3/2}$ and (b) P 2p windows.

of the $Ni_{12}P_5$ particles is further revealed by a HRTEM experiment. Well-defined lattice fringes in $Ni_{12}P_5$ nanoparticles (Figure 2b) suggest the good crystallinity of $Ni_{12}P_5$ nanoparticles, in accordance with that revealed by an XRD experiment. The corresponding reciprocal lattice, the two-dimensional fast Fourier transform (FFT) pattern (inset of Figure 2b), can be indexed to the [−1 4 18] zone axis pattern of tetragonal phase $Ni_{12}P_5$ ($1/d_{OA} = d_{(410)} = 0.21$ nm, $1/d_{OB} = d_{(2-4\ \ 1)} = 0.19$ nm, $\angle AOB = 78°$).

The chemical states of Ni and P in $Ni_{12}P_5$ nanoparticles were investigated by X-ray photoelectron spectroscopy (XPS). The results are shown in Figure 3. Three peaks at 853.1, 856.0, and 860.9 eV are found in the XPS spectrum of the Ni $2p_{3/2}$ window. The peak at 853.1 eV comes from Ni in phosphide, and this binding energy is very close to that of zero valence state Ni (Ni^0, 852.8 eV).[30] It is therefore suggested that the corresponding Ni species have a very small positive charge ($Ni^{\delta+}$, $0 < \delta < 2$). On the other hand, there are two doublets in the spectrum of the P 2p window (129.7 and 132.8 eV). The doublet at 129.7 eV can be assigned to P in phosphide, which suggests that the related P species have a very small negative charge ($P^{\delta-}$, $0 < \delta < 1$), because this binding energy is very close to that of elemental P (130.0 eV).[31] In addition, the peaks at 856.0 and 860.9 eV in the spectrum of the Ni $2p_{3/2}$ window and the doublet at 132.8 eV in the spectrum of the P 2p window are likely to be correlated with nickel phosphate formed on the surface of $Ni_{12}P_5$ due to the exposure of the sample to air.[32] XPS experiments reveal that there are weakly charged species in $Ni_{12}P_5$, including positively charged Ni and negatively charged P.

The HER catalytic activity of $Ni_{12}P_5$ nanoparticles was evaluated by electrochemical experiments. These experiments were carried out in 0.5 M H_2SO_4 aqueous solution (see details in Methods). Prior to electrochemical measurements, OLA was removed from the surface of $Ni_{12}P_5$ nanoparticles by annealing (5% H_2/N_2, 450 °C, 30 min). The removal of OLA was confirmed by the comparison of Fourier transform infrared spectroscopy (FTIR) of the pristine sample and an annealed sample, which showed that the peaks at 2925 and 2855 cm^{-1} corresponding to C−H stretching modes vanish after annealing (Figure S3, Supporting Information). On the other hand, SEM and TEM experiments reveal that annealed particles remain nearly spherical and that the shape of the annealed particles is similar to unannealed ones (panels a−c of Figure S4, Supporting Information). The XRD experiment shows that the annealed particles remain pure $Ni_{12}P_5$ (Figure S4d, Supporting Information). The average diameter estimated from the XRD pattern is 14.8 ± 2.4 nm (Table S3, Supporting Information), suggesting that annealing does not result in an apparent increase in the particle's diameter.

Figure 4a shows the typical polarization curves of $Ni_{12}P_5$ nanoparticle loading on Ti foil ($Ni_{12}P_5$/Ti, loading amount: 3 mg/cm^2), bare Ti foil, commercial Pt/C catalyst (Johnson Matthey, Hispec 3000, 20 wt %) loaded on a glassy carbon electrode (GCE), and bare GCE. Bare Ti foil shows negligible current in the potential range of −200 to 0 mV *versus* the reversible hydrogen evolution potential (RHE). It is obvious that the reductive current in this potential range can be exclusively attributed to the electrocatalytic activity of $Ni_{12}P_5$ particles. The overpotentials required for different electrocatalysts to produce cathodic current densities of 10 and 20 mA/cm^2 (η_{10} and η_{20}) are usually compared in the literature, because under 1 sun AM 1.5 illumination photocathodes usually produce current density of 10−20 mA/cm^2.[4] The η_{10} and η_{20} of the $Ni_{12}P_5$/Ti sample shown in Figure 4a are 107 and 141 mV, respectively. The catalytic activity of $Ni_{12}P_5$ nanoparticles is correlated with their loading amount on Ti foil. Figure S5 (Supporting Information) shows the η_{20} and η_{10} of $Ni_{12}P_5$/Ti with a $Ni_{12}P_5$ loading amount varying from 1 to 3 mg/cm^2. η_{10} decreases gradually from 137 ± 7 mV for 1 mg/cm^2 to 110 ± 3 mV for 3 mg/cm^2, and η_{20} decreases from 175 ± 7 mV for 1 mg/cm^2 to 143 ± 3 mV for 3 mg/cm^2. The optimal η_{20} and η_{10} of $Ni_{12}P_5$ nanoparticles are favorably comparable to most values of reported nonprecious HER electrocatalysts (Table S4, Supporting Information).

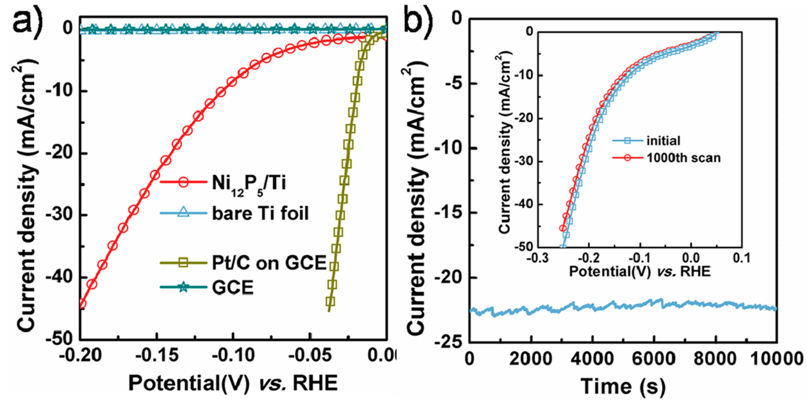

Figure 4. (a) Polarization curves of $Ni_{12}P_5$/Ti, bare Ti foil, Pt/C catalyst loaded on a glassy carbon electrode (GCE), and a bare GCE. The bare Ti foil was annealed under the same conditions as $Ni_{12}P_5$/Ti. The loading amount of the Pt/C catalyst on the GCE is 0.285 mg/cm^2. All potentials in (a) are corrected with an *iR* drop. (b) Current—time relationship recorded in a potentiostatic electrolysis experiment. Inset of (b) shows the polarization curves of the initial scan and 1000th scan of the LSV sweep.

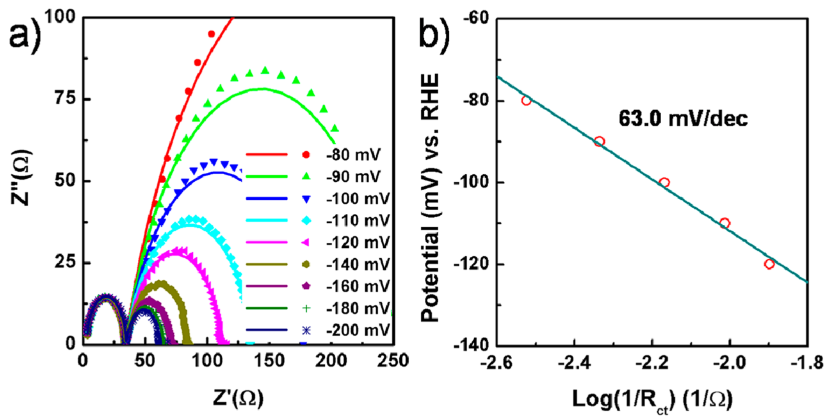

Figure 5. (a) Nyquist plots of EIS data measured in 0.5 M H_2SO_4 solution. (b) Plot of applied potential *versus* inverse R_{ct} on a logarithmic scale.

High durability is of importance for a good electrocatalyst. In our experiments, the stability of $Ni_{12}P_5$ nanoparticles in hydrogen generation was evaluated by potentiostatic electrolysis and accelerated degradation experiments. A potentiostatic electrolysis experiment shows that the current density is nearly maintained in 10 000 s (Figure 4b). An accelerated degradation investigation was carried out by linear sweep voltammetry (LSV). The curve of the 1000th scan almost overlaps the initial one (inset of Figure 4b), and the increase of η_{20} is less than 10 mV after 1000 scans. The potentiostatic electrolysis and LSV experiments suggest the excellent stability of $Ni_{12}P_5$ nanoparticles in HER in 0.5 M H_2SO_4.

The faradaic yield of $Ni_{12}P_5$ was estimated by comparing the theoretical and experimental volumes of H_2 during potentiostatic electrolysis. The theoretical line of H_2 volume was calculated by assuming that all electrons passing through the circuit are totally consumed by the reduction of H^+ into hydrogen (100% faradaic H_2 production). The experimental volume of H_2 during experiment was monitored by water displacement method (see details in Methods). The plots of theoretical and experimental volumes of generated hydrogen versus experiment time are shown in Figure S6 (Supporting Information). The experimental volume matches well the theoretical one in the time scale of electrolysis experiment, suggesting that the faradaic yield of H_2 production is quantitative within the experimental error.

Electrochemical impedance spectroscopy (EIS) experiments were carried out to get further insight into the HER process of $Ni_{12}P_5$ nanoparticles. The results are shown in a Nyquist plot in Figure 5a. These spectra show typical two-time-constant behavior. The semicircles in low frequencies are correlated with a HER process on the surface of $Ni_{12}P_5$ nanoparticles. Smaller diameter corresponds to faster HER kinetics. The diameters of semicircles at low frequencies decrease with increasing overpotential, in accordance with the larger current density at larger potential.

The charge transfer resistance (R_{ct}) at the surface of the catalysts was obtained by data fitting of EIS experimental data with a two-time-constant model equivalent circuit (Figure S7, Supporting Information). The Tafel slope of $Ni_{12}P_5$ nanoparticles was derived from R_{ct} given by EIS data. In the case where the electron transport resistance at the catalyst/substrate interface

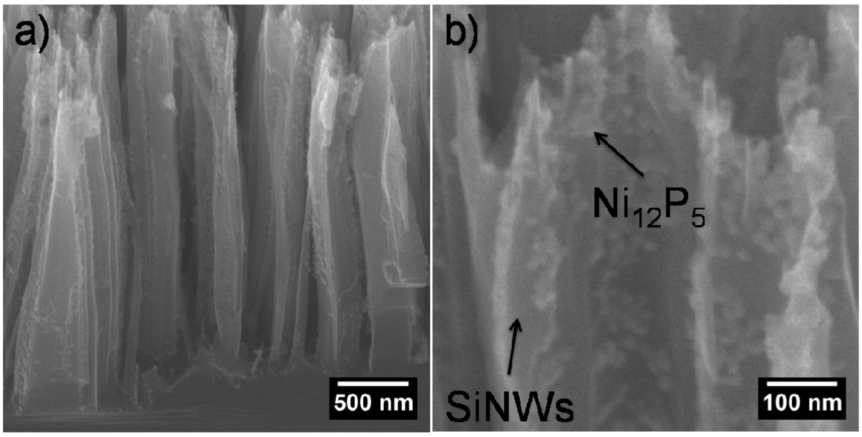

Figure 6. (a) Low- and (b) high-magnification bird's eye view SEM images of $Ni_{12}P_5$/SiNWs. The sample was tilted by 45° in the SEM. SiNWs and $Ni_{12}P_5$ are indicated by arrows in (b), respectively.

or between catalysts is comparable to R_{ct}, the Tafel slope derived from the polarization curve might contain the contribution of electron transport resistance.[33] The Tafel slope can be obtained by the slope of the linear portion in the plot of applied potential *versus* inverse R_{ct} on a logarithmic scale. This approach can exclude the contribution of electron transport resistance. The plot of applied potentials *versus* inverse R_{ct} on a logarithmic scale can be found in Figure 5b, giving a Tafel slope of 63.0 mV/dec.

In the scenario of a classic two-electron-reaction model, the HER process can proceed in two steps: a discharge step (Volmer reaction: $H_3O^+ + e^- \rightarrow H_{ads} + H_2O$) followed by a desorption step (Heyrovsky reaction: $H_{ads} + H_3O^+ + e^- \rightarrow H_2 + H_2O$), or a discharge step followed by a recombination step (Tafel reaction: $H_{ads} + H_{ads} \rightarrow H_2$), where H_{ads} represents a H atom absorbed at the active site of the catalyst. The rate-determining step in the HER process can be assigned to a Volmer, Heyrovsky, or Tafel reaction by a Tafel slope of 116, 38, or 29 mV/dec. The experimental Tafel slope of $Ni_{12}P_5$ nanoparticles (63.0 mV/dec) suggests that the HER on the surface $Ni_{12}P_5$ nanoparticles might follow a Volmer–Heyrovsky mechanism[34] and that the rates of the discharge step and the desorption step might be comparable during the HER process.[35]

The hydride acceptor and proton acceptor are important functional sites in hydrogenase, its analogues ($[Ni(PS3^*)(CO)]^-$ and $[Ni(PNP)_2]^{2+}$), and Ni_2P.[22] The hydride acceptor site (Ni in hydrogenase, $Ni(PS3^*)(CO)]^-$, $[Ni(PNP)_2]^{2+}$, and Ni_2P) is the isolated metal atom that provides moderate bonding to hydrogen, and the hydride acceptor site has a very small positive charge, suggested by calculated total electron density. The proton acceptor site is a nonmetal site having a small negative charge to trap protons (*e.g.*, O of Glu23 in hydrogenase, $-0.44e$; S in $Ni(PS3^*)(CO)]^-$, $-0.4e$; N in $[Ni(PNP)_2]^{2+}$, $-0.34e$; P in Ni_2P, $-0.07e$). These two sites work cooperatively, resulting in high HER catalytic activity.

It has been revealed that Ni and P in $Ni_{12}P_5$ nanoparticles also have small positive and negative charges (Figure 3). The charged natures of Ni and P in $Ni_{12}P_5$ nanoparticles are analogous to those of hydride acceptors and proton acceptors in Ni_2P, [NiFe] hydrogenase, and its analogues, respectively. Such similarity implies that the HER catalytic activity of $Ni_{12}P_5$ nanoparticles might be correlated with the charged natures of Ni and P.

The loading of a HER catalyst onto a photocathode can efficiently promote the HER kinetics on the surface of the photocathode and improve the PCE of the photocathode. This configuration has gained extensive attention. It is valuable to explore whether the loading of $Ni_{12}P_5$ nanoparticles, the new-found HER catalyst, onto a photocathode can result in high-efficiency hydrogen generation.

A simple drop-coating of $Ni_{12}P_5$/hexane dispersion onto SiNWs results in the composite of SiNWs and $Ni_{12}P_5$ nanoparticles. $Ni_{12}P_5$/SiNWs samples were annealed under the same conditions as those used to remove OLA from $Ni_{12}P_5$/Ti. Typical scanning electron microscopy (SEM) images of $Ni_{12}P_5$/SiNWs are shown in Figure 6. $Ni_{12}P_5$ nanoparticles were uniformly distributed on the sidewall of SiNWs, and no apparent aggregation can be found. The diameters of $Ni_{12}P_5$ nanoparticles are smaller than 20 nm, in accordance with those revealed by XRD and TEM.

The typical polarization curves of a sample with optimal performance can be found in Figure 7. Under illumination (100 mW/cm^2), short-circuit current density (J_{sc}), open-circuit potential (V_{oc}), and PCE of $Ni_{12}P_5$/SiNWs sample are 21.0 mA/cm^2, 0.40 V, and 2.97%, respectively. During measurement, copious amounts of gas bubbles evolve from the surface of the $Ni_{12}P_5$/SiNW sample, demonstrating efficient hydrogen generation. On the other hand, the polarization curve measured in the dark shows negligible current in voltage range of -0.1 to 0.4 V *versus* RHE. The unmodified SiNWs sample was also subjected to the same

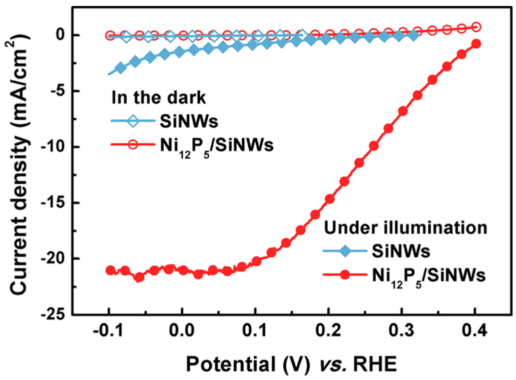

Figure 7. Polarization curves of SiNWs and $Ni_{12}P_5$/SiNWs measured in the dark and under illumination (100 mW/cm^2).

measurement in the dark and under illumination. The J_{sc}, V_{oc}, and PCE of the unmodified SiNW sample are 1.4 mA/cm^2, 0.3 V, and 0.0845%, respectively. The much smaller photoresponse of the unmodified SiNW sample than teh $Ni_{12}P_5$/SiNW sample confirms that $Ni_{12}P_5$ nanoparticles can markedly enhance the photoelectrochemical hydrogen generation capability of SiNWs.

Table S5 (Supporting Information) summarizes the key performance of recently reported Si-based photocathodes. Two typical configurations can be found in these photocathodes. Some photocathodes have a surface n^+ layer and others do not. A surface n^+ layer was introduced to the Si-based photocathode to enhance the separation of photogenerated electrons and holes, and therefore increase the V_{oc} and PCE of the photocathode. The $Ni_{12}P_5$/SiNW sample exhibits the best PCE among photocathodes without a surface n^+ layer. The PCE of the $Ni_{12}P_5$/SiNW sample is larger than that of silicon microwires (SiMWs) decorated with Mo_3S_4 clusters (1.24%),[23] SiNWs decorated with a MoS_2 shell (0.03%),[24] SiNWs modified with MoS_3 particles (2.28%),[26] and p-SiMWs decorated with Pt particles (0.21%).[9] Moreover, it is worth noting that the PCE of the $Ni_{12}P_5$/SiNW sample is larger than that of SiNWs decorated with Pt particles (Pt/SiNWs, 2.73%)[36] and pn^+ SiMWs modified with Ni–Mo particles (2.21%).[25] The direct comparison of the PCE of the $Ni_{12}P_5$/SiNW sample and the Pt/SiNW sample was also carried out in our experimental system. In our experiments the SiNWs were decorated with Pt nanoparticles by electroless plating according to the method introduced in ref 36 (see also the caption of Figure S8, Supporting Information), and the polarization curves of the resulting Pt/SiNW samples are shown in Figure S8 (Supporting Information). It is found that the PCE of the $Ni_{12}P_5$/SiNW sample is also larger than the optimal PCE of the Pt/SiNW sample in our experiments (2.81%). On the other hand, Ni_2P nanoparticles with an 11.2 ± 0.2 nm diameter were also synthesized according to the method introduced in ref 17 (see details in panels a–d of Figure S9, the caption of Figure S9, and Table S6, Supporting Information). The η_{20} of the Ni_2P/Ti sample is 119 mV (Figure S9e, Supporting Information), and the optimal PCE of the Ni_2P/SiNW sample is as large as 3.13 ± 0.07% (Figure S9f and Table S7, Supporting Information). It is therefore suggested that the PCE of SiNWs can be further improved by metal phosphide with better catalytic activity. In addition, the PCE of $Ni_{12}P_5$/SiNWs could also be increased by introduction of an n^+ layer to the surface of the SiNWs.[9] These comparisons demonstrate the promising application of $Ni_{12}P_5$/SiNWs in photoelectrochemical hydrogen generation.

The polarization experiments of $Ni_{12}P_5$ nanoparticles (Figure 4a) have revealed the efficient catalytic activity of $Ni_{12}P_5$ nanoparticles in HER. The enhanced performance of the $Ni_{12}P_5$/SiNW sample in comparison with the unmodified SiNWs sample can therefore be attributed to the HER catalytic activity of $Ni_{12}P_5$ nanoparticles, which increases HER kinetics on the surface of the photocathode.

The performance of $Ni_{12}P_5$/SiNWs is influenced by the loading amount of $Ni_{12}P_5$ nanoparticles. Different amounts of $Ni_{12}P_5$ nanoparticles were deposited onto SiNWs, and the corresponding polarization curves and key parameters are shown in Figure S10 and Table S8 (Supporting Information), respectively. $Ni_{12}P_5$/SiNWs samples with different $Ni_{12}P_5$ loading amounts all exhibit remarkably enhanced PCEs. In particular, the PCE first increases with an increase in the loading amount of $Ni_{12}P_5$ nanoparticles, and further increasing the amount of $Ni_{12}P_5$ nanoparticles decreases the PEC of the $Ni_{12}P_5$/SiNW sample. The optimal PCE can be obtained from a sample loaded with 0.4 mg/cm^2 $Ni_{12}P_5$ nanoparticles. Increasing the amount of $Ni_{12}P_5$ nanoparticles could increase the active sites available for HER, and possibly shields incident illumination. These factors result in an optimal loading amount of catalyst that exhibits the best photoelectrochemical performance.

The stability of a $Ni_{12}P_5$/SiNW photocathode in photoelectrochemical hydrogen generation was evaluated by potentiostatic photoelectrolysis. The result can be found in Figure S11 (Supporting Information). It is shown that the photocurrent density decreases from *ca.* 13.0 mA/cm^2 to 12.6 mA/cm^2 in the first 600 s and then is nearly maintained at 12.6 mA/cm^2 thereafter. The decrease of photocurrent density is likely to be induced by the surface oxidation of SiNWs in the solution. The stability assessment suggests that $Ni_{12}P_5$/SiNWs could work stably in photoelectrochemical hydrogen generation.

CONCLUSIONS

Tetragonal phase $Ni_{12}P_5$ nanoparticles with *ca.* 14 nm diameter were fabricated. $Ni_{12}P_5$ nanoparticles exhibit efficient and stable HER catalytic activity in acidic solution. Typical η_{20} is 143 ± 3 mV. The performance is favorably comparable to those of recently reported non-precious HER catalysts. The HER process follows a Volmer−Heyrovsky mechanism. The HER activity of $Ni_{12}P_5$ nanoparticles might be correlated with the charged natures of Ni and P. The application of $Ni_{12}P_5$ nanoparticles in the photoelectrolysis of water was demonstrated by loading $Ni_{12}P_5$ nanoparticles onto the surface of SiNWs. The PCE of $Ni_{12}P_5$/SiNWs is 2.97%, which is higher than that of unmodified SiNWs (0.0845%) and Pt/SiNWs (2.73% in the literature[36] and 2.81% in our experimental system). The results presented here further demonstrate the promising application potential of metal phosphide in the field of hydrogen generation from electrolysis and photoelectrolysis of water.

METHODS

Reagents. Nickel acetate tetrahydrate (AR), oleylamine (80−90%), and triphenylphosphine (GC) were purchased from Aladdin Reagent and used as received without further purification.

Synthesis of $Ni_{12}P_5$. $Ni(Ac)_2 \cdot 4H_2O$ (0.50 g, 2 mmol) was added to OLA (8 g, 30 mmol) in a 100 mL round-bottom flask. The flask was heated by a heating mantle. The mixture was stirred under a N_2 atmosphere at 120 °C until all $Ni(Ac)_2 \cdot 4H_2O$ was dissolved and a green solution was obtained. Then TPP (2.6 g, 10 mmol) was added into the growth solution, and the flask was filled again with N_2. The temperature of the growth solution was increased to 300 °C and maintained at this value for 30 min. After that, the growth solution was naturally cooled to room temperature. The black product was isolated and washed by repeated centrifugation/ultrasonication treatment, with hexane as good solvent and ethanol as nonsolvent. Finally, the product was dried under vacuum at room temperature.

Fabrication of $Ni_{12}P_5$/Ti. $Ni_{12}P_5$ (32 mg) was dispersed in hexane (1 mL) by ultrasonication (ultrasonic probe, 2 mm diameter, 130 W, 1 h). Different amounts of this dispersion were then dropped onto Ti foil (0.5 cm^2). The resulting $Ni_{12}P_5$/Ti samples were dried under vacuum and subsequently annealed at 450 °C in a 5% H_2/N_2 atmosphere for 30 min. Annealing was carried out in a quartz tube mounted in a tube furnace. The quartz tube was pumped to 20 Pa and filled with nitrogen. This procedure was repeated five times prior to annealing. After annealing, the tube furnace was cooled naturally to room temperature.

Fabrication of $Ni_{12}P_5$/SiNWs. SiNWs were fabricated by metal-assisted chemical etching of silicon wafer.[37,38] A (100)-oriented Si wafer (p type, 1−10 Ω cm) was used for the fabrication of SiNWs. The wafers were degreased by ultrasonication in sequence in ethanol and acetone, each for 15 min, and then rinsed with a copious amount of deionized water. After that, the degreased Si substrates were subjected to a boiling solution composed of H_2O_2 and H_2SO_4 (1:4, v/v) for 30 min, then rinsed with deionized water. The clean Si substrates were etched in aqueous etchant containing $AgNO_3$ (20 mM) and HF (4.5 mM) for 30 min. Afterward, the etched Si substrates were immersed in 5% HNO_3 aqueous solution for 30 min to remove surface silver dendrites. The resulting SiNW samples were rinsed with deionized water and finally dried at 80 °C in air. $Ni_{12}P_5$/SiNW samples were obtained by a method similar to that for $Ni_{12}P_5$/Ti samples, except that a lower concentration of $Ni_{12}P_5$/hexane dispersion (10 mg/mL) was used.

Characterization. The morphologies of $Ni_{12}P_5$ and $Ni_{12}P_5$/SiNWs were accessed by SEM (JSM7001F, JEOL) and TEM (JEM2100, JEOL). The chemical composition of $Ni_{12}P_5$ was determined by an EDX spectrum in an INCA system (Oxford Instruments) equipped on a JSM7001F. For TEM investigation, $Ni_{12}P_5$ particles were dispersed in hexane by ultrasonication. The dispersion was dropped onto a carbon-coated copper grid (300-mesh). The copper grid was then dried at 100 °C for 5 min before the TEM characterization.

XRD experiments were carried out on a D8 Advance with graphite-monochromatized Cu Kα radiation (λ = 1.54178 Å). The XPS spectra were collected by an ESCALAB250Xi System (ThermoFisher) equipped with a monochromatic Al Kα (1486.6 eV) source and a concentric hemispherical energy analyzer.

Electrochemical Performance. All electrochemical measurements were carried out with an electrochemical workstation (CHI 614D, CH Instrument) in a three-electrode configuration, with $Ni_{12}P_5$/Ti or $Ni_{12}P_5$/SiNWs as working electrode, a graphite rod (6 mm diameter) as counter electrode, and a mercury/mercurous sulfate electrode (MSE) as reference electrode. $Ni_{12}P_5$/Ti or $Ni_{12}P_5$/SiNW samples were assembled into a homemade electrochemical cell, with only a defined area (0.07 cm^2) of the front surface of the sample exposed to solution during measurements. The Pt/C catalyst (4 mg) and Nafion solution (5 wt %, 80 μL) were dispersed in 1 mL of water/ethanol (4:1, v/v) by ultrasonication (ultrasonic probe, 2 mm diameter, 130 W, 1 h) to form a homogeneous ink. Then 5 μL of catalyst ink was loaded onto a glassy carbon electrode (3 mm diameter).

H_2SO_4 (0.5 M) aqueous solution was used in the measurement of $Ni_{12}P_5$/Ti samples, and H_2SO_4 (0.05 M) aqueous solution containing 0.5 M K_2SO_4 was used for the measurement of $Ni_{12}P_5$/SiNW samples. The solutions were purged with high-purity H_2 for 30 min prior to electrochemical measurements. The RHE was determined by open-circuit potential of a clean Pt electrode in corresponding solutions,[4,9] being −0.694 V *vs* MSE for a 0.5 M H_2SO_4 solution and −0.762 V *vs* MSE for a solution containing 0.05 M H_2SO_4 and 0.5 M K_2SO_4.

Polarization curves of the $Ni_{12}P_5$/Ti sample were measured at a 5 mV/s sweep rate in a rigorously stirred solution (1600 rpm). The uncompensated cell resistance (R) was determined by the current-interrupt method, and the experimental potential is corrected by subtracting the ohmic drop (iR), where i is the current. The potentiostatic electrolysis was carried out at −0.15 V *vs* RHE. For accelerated degradation investigation, LSV measurement was carried out with a 50 mV/s sweep rate between −0.25 and 0.05 V *vs* RHE without accounting for uncompensated resistance. Electrochemical impedance spectroscopy measurements were carried out at different potentials in the frequency range of 10^{-2} to 10^6 Hz with 10 mV sinusoidal perturbations and 12 steps per decade in a 0.5 M H_2SO_4 solution. The Tafel slope of the $Ni_{12}P_5$/Ti sample was obtained by fitting experimental data with the equation $\eta = a + b \log(1/R_{ct})$, where η is the overpotential, b is the Tafel slope, and R_{ct} is the charge transfer resistance derived from EIS data.

The volume of H_2 during the potentiostatic electrolysis experiment was monitored by the water displacement method using a configuration shown in Figure S12 (Supporting Information). In this experiment, the back side of the Ti foil was connected to a Cu wire with Ag paste. The Cu wire was threaded to a glass tube (6 mm diameter), and the back side and front side of the sample electrode were then sealed with epoxy resin with the exception of an exposed area (∼0.5 cm^2). A Freescale MPXV7002DP differential pressure transducer was employed to monitor pressure variation in the gas-gathering tube, and then the volume of generated H_2 was computed from pressure variation in the gas-gathering tube (see details in the Supporting Information). The current and charge passing the $Ni_{12}P_5$ were measured with the electrochemical workstation, and the voltage change of the differential pressure transducer was monitored with a digital multimeter ($4^1/_2$ digits). Prior to experiment, the relationship between volume of gathered gas and the variation of output voltage of the differential pressure transducer (*i.e.*, pressure variation in the gas-gathering tube) was calibrated by injecting a known amount of air into the gas-gathering tube and recording the variation of output voltage of the differential pressure transducer.

In the photoelectrochemical measurement of $Ni_{12}P_5$/SiNW samples, indium−gallium alloy (99.99%, Sigma-Aldrich) was applied to the back side of SiNWs for ohmic contact. The illumination was generated by a xenon lamp (350 W), and the incident light density was adjusted to 100 mW/cm^2 prior to each experiment. Photocurrent density−potential (J−E) relations were measured at a 50 mV/s scan rate. The V_{oc}, J_{sc}, PCE, and fill factor were derived from polarization curves according to the formula defined in ref 4.

Conflict of Interest: The authors declare no competing financial interest.

Acknowledgment. This research was financially supported by the National Natural Science Foundation of China (61006049, 50925207), the Ministry of Science and Technology of China (2011DFG52970), the Ministry of Education of China (IRT1064), 111 Project (B13025), Jiangsu Innovation Research Team, Jiangsu Province (2011-XCL-019 and 2013-479), and Natural Science Foundation of Jiangsu.

Supporting Information Available: Estimation of particle diameter from XRD patterns, additional EDX spectrum, SAED patterns, FTIR spectra of $Ni_{12}P_5$ particles, SEM images of unannealed and annealed $Ni_{12}P_5$/Ti samples, TEM image and XRD patterns of annealed $Ni_{12}P_5$ particles, plots of η_{20} and η_{10} *versus* loading amount of $Ni_{12}P_5$ nanoparticles, list of HER performances of recently reported nonprecious HER catalysts, comparison of theoretical and experimental volumes of generated hydrogen during a potentiostatic electrolysis experiment, two-time-constant model equivalent circuit used for the fitting of EIS data, list of key performances of photocathodes loaded with various catalysts, polarization curves of Pt/SiNW samples with different electroless deposition times of Pt particles, polarization curves of SiNWs loaded with different amounts of $Ni_{12}P_5$, list of key performances of $Ni_{12}P_5$/SiNW samples with different loading amounts of $Ni_{12}P_5$, current−time relationship in a potentiostatic electrolysis experiment of a $Ni_{12}P_5$/SiNW sample under illumination, and illustration of the setup used to monitor the volume of generated gas. This material is available free of charge *via* the Internet at http://pubs.acs.org.

REFERENCES AND NOTES

1. Bockris, J. O. M. The Origin of Ideas on a Hydrogen Economy and Its Solution to the Decay of the Environment. *Int. J. Hydrogen Energy* **2002**, *27*, 731–740.
2. Armaroli, N.; Balzani, V. The Hydrogen Issue. *ChemSusChem* **2011**, *4*, 21–36.
3. Mao, S. S.; Chen, X. B. Selected Nanotechnologies for Renewable Energy Applications. *Int. J. Energy Res.* **2007**, *31*, 619–636.
4. Walter, M. G.; Warren, E. L.; McKone, J. R.; Boettcher, S. W.; Mi, Q. X.; Santori, E. A.; Lewis, N. S. Solar Water Splitting Cells. *Chem. Rev.* **2010**, *110*, 6446–6473.
5. Cook, T. R.; Dogutan, D. K.; Reece, S. Y.; Surendranath, Y.; Teets, T. S.; Nocera, D. G. Solar Energy Supply and Storage for the Legacy and Nonlegacy Worlds. *Chem. Rev.* **2010**, *110*, 6474–6502.
6. Dominey, R. N.; Lewis, N. S.; Bruce, J. A.; Bookbinder, D. C.; Wrighton, M. S. Improvement of Photoelectrochemical Hydrogen Generation by Surface Modification of p-Type Silicon Semiconductor Photocathodes. *J. Am. Chem. Soc.* **1982**, *104*, 467–482.
7. Szklarczyk, M.; Bockris, J. O. M. Photoelectrocatalysis on Silicon in Solar Light. *Appl. Phys. Lett.* **1983**, *42*, 1035.
8. Szklarczyk, M.; Bockris, J. O. M. Photoelectrocatalysis and Electrocatalysis on p-Silicon. *J. Phys. Chem.* **1984**, *88*, 1808–1815.
9. Boettcher, S. W.; Warren, E. L.; Putnam, M. C.; Santori, E. A.; Turner-Evans, D.; Kelzenberg, M. D.; Walter, M. G.; McKone, J. R.; Brunschwig, B. S.; Atwater, H. A.; *et al.* Photoelectrochemical Hydrogen Evolution Using Si Microwire Arrays. *J. Am. Chem. Soc.* **2011**, *133*, 1216–1219.
10. Hinnemann, B.; Moses, P. G.; Bonde, J.; Jørgensen, K. P.; Nielsen, J. H.; Horch, S.; Chorkendorff, I.; Nørskov, J. K. Biomimetic Hydrogen Evolution: MoS_2 Nanoparticles as Catalyst for Hydrogen Evolution. *J. Am. Chem. Soc.* **2005**, *127*, 5308–5309.
11. Merki, D.; Fierro, S.; Vrubel, H.; Hu, X. L. Amorphous Molybdenum Sulfide Films as Catalysts for Electrochemical Hydrogen Production in Water. *Chem. Sci.* **2011**, *2*, 1262–1267.
12. Ivanovskaya, A.; Singh, N.; Liu, R. F.; Kreutzer, H.; Baltrusaitis, J.; Nguyen, T. V.; Metiu, H.; McFarland, E. Transition Metal Sulfide Hydrogen Evolution Catalysts for Hydrobromic Acid Electrolysis. *Langmuir* **2013**, *29*, 480–492.
13. Kong, D. S.; Cha, J. J.; Wang, H. T.; Lee, H. R.; Cui, Y. First-Row Transition Metal Dichalcogenide Catalysts for Hydrogen Evolution Reaction. *Energy Environ. Sci.* **2013**, *6*, 3553–3558.
14. Vrubel, H.; Hu, X. L. Molybdenum Boride and Carbide Catalyze Hydrogen Evolution in both Acidic and Basic Solutions. *Angew. Chem., Int. Ed.* **2012**, *51*, 12703–12706.
15. Chen, W. F.; Wang, C. H.; Sasaki, K.; Marinkovic, N.; Xu, W.; Muckerman, J. T.; Zhu, Y.; Adzic, R. R. Highly Active and Durable Nanostructured Molybdenum Carbide Electrocatalysts for Hydrogen Production. *Energy Environ. Sci.* **2013**, *6*, 943–951.
16. Harnisch, F.; Sievers, G.; Schröder, U. Tungsten Carbide as Electrocatalyst for the Hydrogen Evolution Reaction in pH Neutral Electrolyte Solutions. *Appl. Catal. B: Environ.* **2009**, *89*, 455–458.
17. Popczun, E. J.; McKone, J. R.; Read, C. G.; Biacchi, A. J.; Wiltrout, A. M.; Lewis, N. S.; Schaak, R. E. Nanostructured Nickel Phosphide as an Electrocatalyst for the Hydrogen Evolution Reaction. *J. Am. Chem. Soc.* **2013**, *135*, 9267–9270.
18. Popczun, E. J.; Read, C. G.; Roske, C. W.; Lewis, N. S.; Schaak, R. E. Highly Active Electrocatalysis of the Hydrogen Evolution Reaction by Cobalt Phosphide Nanoparticles. *Angew. Chem., Int. Ed.* **2014**, *53*, 5427–5430.
19. Tian, J. Q.; Liu, Q.; Asiri, A. M.; Sun, X. P. Self-Supported Nanoporous Cobalt Phosphide Nanowire Arrays: An Efficient 3D Hydrogen-Evolving Cathode over the Wide Range of pH 0−14. *J. Am. Chem. Soc.* **2014**, *136*, 7587–7590.
20. Liu, Q.; Tian, J. Q.; Cui, W.; Jiang, P.; Cheng, N. Y.; Asiri, A. M.; Sun, X. P. Carbon Nanotubes Decorated with CoP Nanocrystals: A Highly Active Non-Noble-Metal Nanohybrid Electrocatalyst for Hydrogen Evolution. *Angew. Chem., Int. Ed.* **2014**, *53*, 6710–6714.
21. Esposito, D. V.; Hunt, S. T.; Kimmel, Y. C.; Chen, J. G. G. A New Class of Electrocatalysts for Hydrogen Production from Water Electrolysis: Metal Monolayers Supported on Low-Cost Transition Metal Carbides. *J. Am. Chem. Soc.* **2012**, *134*, 3025–3033.
22. Liu, P.; Rodriguez, J. A. Catalysts for Hydrogen Evolution from the [NiFe] Hydrogenase to the Ni_2P(001) Surface: The Importance of Ensemble Effect. *J. Am. Chem. Soc.* **2005**, *127*, 14871–14878.
23. Hou, Y. D.; Abrams, B. L.; Vesborg, P. C. K.; Bjorketun, M. E.; Herbst, K.; Bech, L.; Setti, A. M.; Damsgaard, C. D.; Pedersen, T.; Hansen, O.; *et al.* Bioinspired Molecular co-Catalysts Bonded to a Silicon Photocathode for Solar Hydrogen Evolution. *Nat. Mater.* **2011**, *10*, 434–438.
24. Tran, P. D.; Pramana, S. S.; Kale, V. S.; Nguyen, M.; Chiam, S. Y.; Batabyal, S. K.; Wong, L. H.; Barber, J.; Loo, J. Novel Assembly of an MoS_2 Electrocatalyst onto a Silicon Nanowire Array Electrode to Construct a Photocathode Composed of Elements Abundant on the Earth for Hydrogen Generation. *Chem.—Eur. J.* **2012**, *18*, 13994–13999.
25. Seger, B.; Laursen, A. B.; Vesborg, P. C. K.; Pedersen, T.; Hansen, O.; Dahl, S.; Chorkendorff, I. Hydrogen Production Using a Molybdenum Sulfide Catalyst on a Titanium-Protected n+p-Silicon Photocathode. *Angew. Chem., Int. Ed.* **2012**, *51*, 9128–9131.
26. Huang, Z. P.; Wang, C. F.; Pan, L.; Tian, F.; Zhang, X. X.; Zhang, C. Enhanced Photoelectrochemical Hydrogen Production Using Silicon Nanowires@MoS_3. *Nano Energy* **2013**, *2*, 1337–1346.
27. McKone, J. R.; Warren, E. L.; Bierman, M. J.; Boettcher, S. W.; Brunschwig, B. S.; Lewis, N. S.; Gray, H. B. Evaluation of Pt, Ni, and Ni-Mo Electrocatalysts for Hydrogen Evolution on Crystalline Si Electrodes. *Energy Environ. Sci.* **2011**, *4*, 3573–3583.

28. Warren, E. L.; McKone, J. R.; Atwater, H. A.; Gray, H. B.; Lewis, N. S. Hydrogen-Evolution Characteristics of Ni-Mo-Coated, Radial Junction, n+p-Silicon Microwire Array Photocathodes. *Energy Environ. Sci.* **2012**, *5*, 9653–9661.
29. Borchert, H.; Shevchenko, E. V.; Robert, A.; Mekis, I.; Kornowsk, A.; Grübel, G.; Weller, H. Determination of Nanocrystal Sizes: A Comparison of TEM, SAXS, and XRD Studies of Highly Monodisperse $CoPt_3$ Particles. *Langmuir* **2005**, *21*, 1931–1936.
30. Mandale, A. B.; Badrinarayanan, S.; Date, S. K.; Sinha, A. P. B. Photoelectron-Spectroscopic Study of Nickel, Manganese and Cobalt Selenides. *J. Electron Spectrosc. Relat. Phenom.* **1984**, *33*, 61–72.
31. Nefedov, V. I.; Salyn, Y. V.; Domashevskaya, E. P.; Ugai, Y. A.; Terekhov, V. A. A Study by XPS and XRS of the Participation in Chemical Bonding of the 3d Electrons of Copper, Zinc and Gallium. *J. Electron Spectrosc. Relat. Phenom.* **1975**, *6*, 231–238.
32. Sawhill, S. J.; Layman, K. A.; Van Wyk, D. R.; Engelhard, M. H.; Wang, C.; Bussell, M. E. Thiophene Hydrodesulfurization over Nickel Phosphide Catalysts: Effect of the Precursor Composition and Support. *J. Catal.* **2005**, *231*, 300–313.
33. Vrubel, H.; Moehl, T.; Gratzel, M.; Hu, X. Revealing and Accelerating Slow Electron Transport in Amorphous Molybdenum Sulphide Particles for Hydrogen Evolution Reaction. *Chem. Commun.* **2013**, *49*, 8985–8987.
34. Chen, W. F.; Iyer, S.; Iyer, S.; Sasaki, K.; Wang, C. H.; Zhu, Y. M.; Muckerman, J. T.; Fujita, E. Biomass-Derived Electrocatalytic Composites for Hydrogen Evolution. *Energy Environ. Sci.* **2013**, *6*, 1818–1826.
35. Gao, M. R.; Lin, Z. Y.; Zhuang, T. T.; Jiang, J.; Xu, Y. F.; Zheng, Y. R.; Yu, S. H. Mixed-Solution Synthesis of Sea Urchin-Like NiSe Nanofiber Assemblies as Economical Pt-Free Catalysts for Electrochemical H_2 Production. *J. Mater. Chem.* **2012**, *22*, 13662–13668.
36. Oh, I.; Kye, J.; Hwang, S. Enhanced Photoelectrochemical Hydrogen Production from Silicon Nanowire Array Photocathode. *Nano Lett.* **2011**, *12*, 298–302.
37. Huang, Z. P.; Geyer, N.; Werner, P.; de Boor, J.; Gosele, U. Metal-Assisted Chemical Etching of Silicon: A Review. *Adv. Mater.* **2011**, *23*, 285–308.
38. Peng, K. Q.; Yan, Y. J.; Gao, S. P.; Zhu, J. Synthesis of Large-Area Silicon Nanowire Arrays *via* Self-Assembling Nanoelectrochemistry. *Adv. Mater.* **2002**, *14*, 1164–1167.